J Mater Sci (2019) 54:14157–14170

Materials for life sciences

Fabrication and characterization of high efficient Z-scheme photocatalyst Bi_2MoO_6/reduced graphene oxide/BiOBr for the degradation of organic dye and antibiotic under visible-light irradiation

Rui Zhang[1], Qiong Han[1,*], Yu Li[1], Tongqing Zhang[1], Yi Liu[1], Kunlin Zeng[1], and Chen Zhao[1]

[1] College of Chemistry and Chemical Engineering, Southwest Petroleum University, Chengdu 610500, Sichuan, People's Republic of China

Received: 6 June 2019
Accepted: 24 July 2019
Published online: 31 July 2019

ABSTRACT

A novel Bi_2MoO_6/reduced graphene oxide/BiOBr (Bi_2MoO_6/RGO/BiOBr) composite was successfully synthesized via a facile solvothermal synthesis and precipitation method. The Bi_2MoO_6/RGO/BiOBr composite was characterized by X-ray diffraction, X-ray photoelectron spectroscopy, scanning electron microscopy, transmission electron microscopy, UV–vis diffuse reflectance spectroscopy (UV–vis DRS) and photoelectrochemical measurements. The photocatalytic properties were explored for removal of methylene blue (MB) and norfloxacin (NFX) under visible-light irradiation. The Bi_2MoO_6/RGO/BiOBr composite exhibits the highest degradation rate compared with Bi_2MoO_6, BiOBr and Bi_2MoO_6/BiOBr composite, and that removal ratios of MB and NFX were 96.93% and 78.12%, respectively. A Z-scheme catalytic mechanism suitable for the system was proposed based on the results of UV–vis DRS, free radical trapping experiments and *M–S* carve analysis, in which RGO as an electronic medium can accelerate electron transfer. It is noteworthy that the close contact interface structure promotes the separation of electrons and holes and improves the photocatalytic performance.

Introduction

The rapid development of science and technology has caused serious pollution and destruction to the environment. A large number of toxic and harmful pollutants are accumulating and transforming in soil, air and water, posing a great threat to ecological balance and human physical as well as mental health [1]. Therefore, the development of efficient environmental protection treatment technology has become a research hotspot in recent years. Semiconductor photocatalysis has many advantages, such as large

Address correspondence to E-mail: 1032841867@qq.com

https://doi.org/10.1007/s10853-019-03883-0

treatment range, high efficiency, energy saving, cleanliness, non-toxicity, no secondary pollution as well as simple process, and hence is regarded as an environmentally friendly green technology [2]. However, it is still a problem to develop efficient photocatalysts in practical applications due to the low yield of quantum and light. Recently, researchers have synthesized a large number of composite semiconductor materials such as $BiOBr/TiO_2$ [3], Bi_2MoO_6/TiO_2 [4] and $g\text{-}C_3N_4/TiO_2$ [5] based on traditional photocatalyst TiO_2.

BiOBr, a layered flower structure has a large surface area and high permeability with a moderate energy gap of 2.5 eV, is attracting widespread attentions. What is more important is that BiOBr has a high oxidation ability and can be effectively used for pollutants photodegradation because its valence band (about 3.19 eV) [6] is much higher than that of traditional photocatalysts or oxidants. However, there are still some shortcomings such as the high recombination rate of photogenerated electrons and holes, and the low quantum efficiency limits the practical application in water treatment. It has been reported that the combination of other semiconductor and BiOBr [7–10] is the most effective way to improve the catalytic activity. For example, the heterojunction composed of $BiOBr/CeO_2$ [11], BiOBr/ZnO [12] and $BiOBr/Bi_2O_3$ [13] can effectively slow down the electron–hole recombination and adjust the visible-light response range, thus improving the photocatalytic activity of BiOBr.

It is reported that Bi_2MoO_6 as an *Aurivillius*-type oxide with perovskite layered structure is formed by octahedral MoO_6 layers embedded in $[Bi_2O_2]^{2+}$ layers [14]. The conduction band is composed of Mo 4*d* orbital, and valence band is composed of O 2*p* and Bi 6*s* orbital hybridization [15]. There is a found that the maximum absorption wavelength of Bi_2MoO_6 is 520 nm under visible light, showing excellent visible-light catalytic performance in decomposing and degrading organic pollutants in water. However, it has been restricted in practical applications because of its low absorption efficiency and quantum yield of visible light [16]. Therefore, Bi_2MoO_6 will also be combined with other semiconductors to improve the utilization of solar energy and photocatalytic activity.

A Z-scheme photocatalyst [17–19] based on Bi_2MoO_6/RGO/BiOBr ternary composite was prepared by hydrothermal method in the present study. The structure and morphology of the as-prepared photocatalyst were characterized. The addition of Bi_2MoO_6 and RGO makes the photocatalyst have higher separation efficiency of electron–hole pairs than pure BiOBr. Afterward, the photocatalytic properties of the composite were studied via degradation of dyes and antibiotics (NFX) under visible light. Thus, this work provides a new type of Z-scheme photocatalyst which can effectively and cleanly remove organic pollutants under visible light.

Experimental

Materials

Absolute ethyl alcohol(C_2H_5OH), graphite powder, potassium permanganate($KMnO_4$), sulfuric acid(H_2SO_4), phosphoric acid(H_3PO_4), hydrochloric acid(HCl), hydrogen peroxide(H_2O_2), ammonium molybdate ($(NH_4)_6Mo_7O_{24}\cdot 4H_2O$), bismuth nitrate pentahydrate ($Bi(NO_3)_3\cdot 5H_2O$), ammonia ($NH_3\cdot H_2O$), sodium bromide (NaBr), isopropyl alcohol (IPA), *p*-benzoquinone (BQ), ethylenediamine tetraacetic acid disodium (EDTA-2Na) and methylene blue (MB) were purchased from Kelong chemical reagent factory (Chengdu, China). All reagents were of analytical grade, and the experimental water was deionized water.

Synthesis of Bi_2MoO_6 and Bi_2MoO_6/RGO

In this paper, GO was prepared by the modified Hummers method [20]. The Bi_2MoO_6/RGO was prepared by a hydrothermal method. In a typical process, 30 mg GO was dispersed into 30 ml deionized water by ultrasonic, and then, 5 mmol $Bi(NO_3)_3\cdot 5H_2O$ was dissolved into GO dispersion solution, stirred for 30 min. The 0.024 mol/L $(NH_4)_6Mo_7O_{24}\cdot 4H_2O$ solution (30 ml) was slowly dropped into the above solution under stirring. Subsequently, the ammonia solution was dropped to adjust the pH of the mixed solution to 6, the reaction solution was transferred to the teflon-lined stainless steel autoclave and reacted at 140 °C for 12 h [21]. The precipitates were centrifuged and collected after the autoclave was cooled naturally, and washed three times with absolute ethanol and deionized water. Finally, the precipitates were dried in oven at 60 °C for 12 h to obtain Bi_2MoO_6/RGO. For comparison,

the pure Bi_2MoO_6 was prepared under the same conditions without adding GO.

Preparation of BiOBr, Bi_2MoO_6/BiOBr and Bi_2MoO_6/RGO/BiOBr

The Bi_2MoO_6/RGO/BiOBr composite was prepared by precipitation method [22]. In detail, the as-prepared Bi_2MoO_6/RGO powder (89.78 mg) was dispersed in 30 ml deionized water to form a uniform solution by ultrasound. Then, 0.4365 g $Bi(NO_3)_3$-$5H_2O$ was added into the above dispersion, followed by 0.0927 g NaBr and stirred at room temperature for 24 h. The precipitates were collected by centrifugation and washed with absolute ethanol and deionized water for three times, and then dried in oven at 60 °C for 12 h. The obtained product was 0.1Bi_2MoO_6/RGO/BiOBr [23]. The different molar ratio of composites were prepared and labeled 0.2Bi_2MoO_6/RGO/BiOBr and 0.05Bi_2MoO_6/RGO/BiOBr by changing the addition of Bi_2MoO_6/RGO, and the pure BiOBr and Bi_2MoO_6/BiOBr were prepared without adding Bi_2MoO_6/RGO and replacing the Bi_2MoO_6/RGO precursor with Bi_2MoO_6, respectively (Scheme 1).

Characterization

The X-ray diffraction patterns of the photocatalysts were analyzed by X-ray diffractometer (X'Pert PRO MRD, Panako, Netherlands) with diffraction angle 2θ = 5°–80°. The X-ray photoelectron spectroscopy (XPS) analysis was carried out with a K-Alpha$^+$ X-ray photoelectron spectrometer (Thermo fisher Scientific). The surface morphology of the samples was observed by scanning electron microscopy (SEM, ZEISS EV0 MA15, Germany) and transmission electron microscopy (TEM, Joel-2100F, Japan). The UV–Vis diffuse reflectance spectroscopy in the range of 200-800 nm was recorded by UV–vis spectrophotometer (PerkinElmer Lambda 850, America). Photoluminescence spectra (PL) of the as-prepared catalysts were investigated by fluorescence spectrometer (PerKinElmer LS55, America) with the emission wavelength at 325 nm.

Photocatalytic performance evaluation

The 50 mg photocatalyst was dispersed into 50 ml MB solution (20 mg/L) and NFX solution (10 mg/L) by ultrasonic, respectively. Subsequently, the suspension was stirred in darkness for 30 min to establish adsorption–desorption equilibrium [24]. A high-pressure mercury lamp with a 420 nm cutoff filter was used as the light source. The 3 ml suspension was centrifuged at 5 min intervals during irradiation, and the supernatant was determined using Hitachi UV1800 UV–vis spectrophotometer. The maximum absorption wavelengths of MB and NFX are 664 and 278 nm, respectively. The photocatalytic degradation rate η can be calculated by the following formula (1):

$$\eta = \frac{C_0 - C_t}{C_0} \times 100\% \quad (1)$$

where C_0 and C_t are the pollutant concentration of the initial and after irradiation for t time (min), respectively. Meanwhile, the free radical capture experiments were carried out in the same process as photodegradation experiments. After reaching adsorption–desorption equilibrium, the isopropanol (IPA, 10 mmol/L), para-benzoquinone (BQ, 10 mmol/L) and ethylenediamine tetraacetic acid disodium (EDTA-2Na, 1 mmol/L) were added into the reaction system, which acted as scavenger for capturing hydroxyl radicals (·OH), superoxide radicals ($\cdot O_2^-$) and photogenerated holes (h^+) [25], respectively.

Photoelectrochemical measurements

The photoelectrochemical properties of the samples were tested by CHI 660E electrochemical workstation (CHI Co., China). A Pt electrode, standard calomel electrode and FTO electrode are used as opposite electrode, reference electrode and working electrode, respectively. Firstly, 10 mg photocatalyst and 200 µl 5% naphthol solution were added to 600 µl absolute ethanol, and sonicated for 30 min to form a uniform solution. The dispersion was dropped on the conductive surface of FTO glass electrode and ventilated as well as dried overnight at room temperature. A 200-W high-pressure mercury lamp with a 420 nm cutoff filter was used as the light source, and the electrolyte solution was 0.5 mol/L Na_2SO_4 aqueous solution.

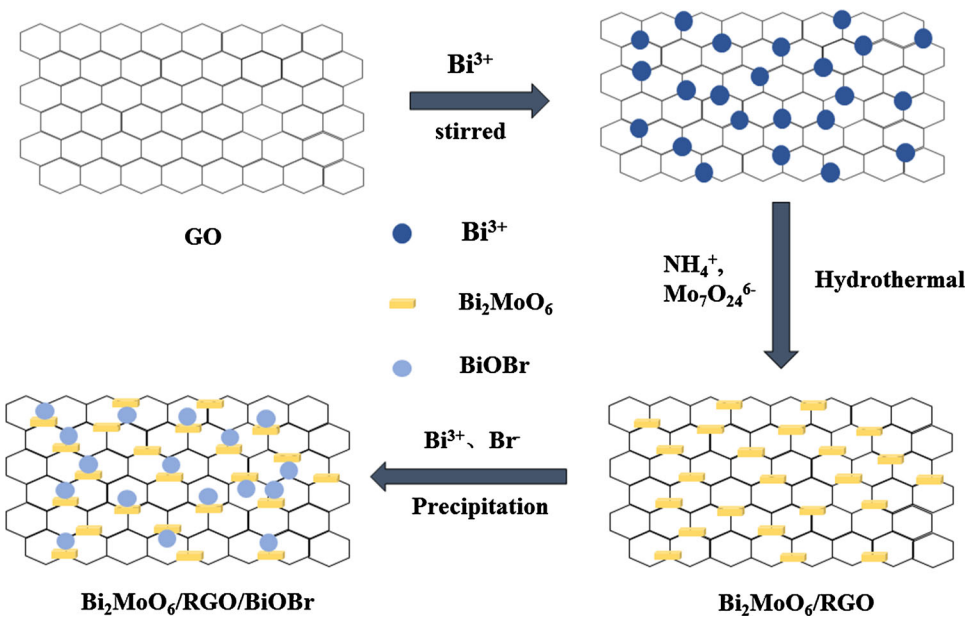

Scheme 1 Preparation mechanism diagram of Bi_2MoO_6/RGO/BiOBr.

Results and discussion

Structural analysis

The crystal structure and phase composition of the samples were determined by XRD. The XRD spectra of BiOBr, Bi_2MoO_6, Bi_2MoO_6/BiOBr and Bi_2MoO_6/RGO/BiOBr are presented in Fig. 1. The main peaks of the BiOBr diffraction pattern located at 10.82°, 21.91°, 25.22°, 31.84°, 32.17°, 33.21°, 39.5°, 44.84°, 50.63°, 56.25°, 57.24°, 69.61° and 76.63° are indexed to the diffraction surfaces (001), (002), (011), (012), (004), (003), (112), (014), (114), (212), (211) and (310) of the tetragonal phase of BiOBr (JCPDS 09-0393) [26], respectively. For pure Bi_2MoO_6, the (020), (131), (060), (260), (331) and (262) crystal planes corresponding to the diffraction angles at 10.85°, 28.26°, 32.65°, 46.86°, 55.58° and 58.43°, respectively, which are in good agreement with the standard orthorhombic phase Bi_2MoO_6 card (JCPDS 76-2388) [27]. All the diffraction peaks of Bi_2MoO_6/BiOBr and Bi_2MoO_6/RGO/BiOBr heterojunctions with different Bi_2MoO_6 molar ratios are the same as those of pure BiOBr basically, and the diffraction peaks of Bi_2MoO_6 can be observed at (131) crystal plane. Moreover, the diffraction peak of Bi_2MoO_6 increases obviously with the increase of Bi_2MoO_6 content and there are no other impurity diffraction peaks. However, it is difficult to observe RGO characteristic peaks, which may be due to the low content of RGO and the high dispersion in the

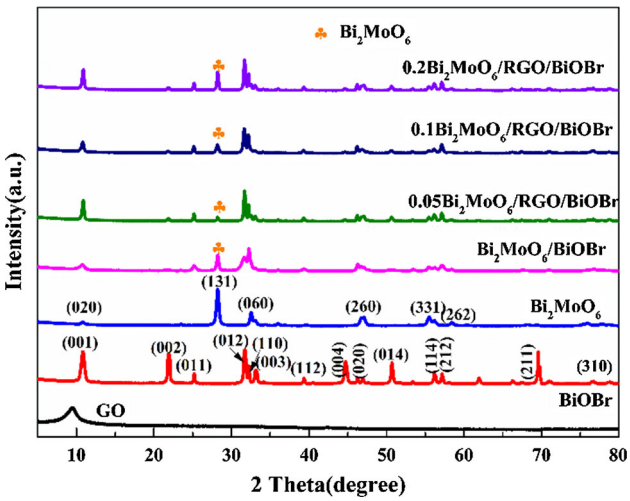

Figure 1 The XRD spectra of BiOBr, Bi_2MoO_6, Bi_2MoO_6/BiOBr and Bi_2MoO_6/RGO/BiOBr composite with different molar ratios of Bi_2MoO_6.

composite, indicating that GO is partially reduced to RGO [28].

The chemical composition and valence states of the elements on the composite surface were analyzed by XPS spectra. As presented in the full spectrum of XPS (Fig. 2a), it can be seen that the composite surface is mainly composed of Bi, Br, O, Mo and C elements. The high-resolution XPS spectra (HRXPS) of Bi 4*f*, Br 3*d*, O 1*s*, Mo 3*d* and C 1*s* were shown in Fig. 2b–f. From the Bi 4*f* image (Fig. 2b), the peaks of Bi $4f_{5/2}$ and Bi $4f_{7/2}$ appeared at 165.01 and 159.70 eV, respectively, which indicated that Bi^{3+} existed mainly

in the composite [29]. Then, the peaks centered on 69.22 and 67.69 eV are Br $3d_{3/2}$ and Br $3d_{5/2}$ [30, 31], respectively. As shown in Fig. 2d, the O 1*s* spectra can be fitted to three peaks at 533.29, 531.86 and 530.07 eV, which are assigned to O–C=O, C–O and O_2^- anion, respectively. It can be seen from Fig. 2e that the location at 235.85 and 232.68 eV are characteristic peaks of Mo $3d_{3/2}$ and Mo $3d_{5/2}$, respectively, indicating that Mo element exists mainly in the form of Mo^{6+} in the Bi_2MoO_6/RGO/BiOBr composite [32, 33]. Moreover, the spectra of C 1s in Bi_2MoO_6/RGO/BiOBr composite are shown in Fig. 2f, and the spectra can be fitted into three peaks at 288.40, 286.33 and 284.56 eV, which are

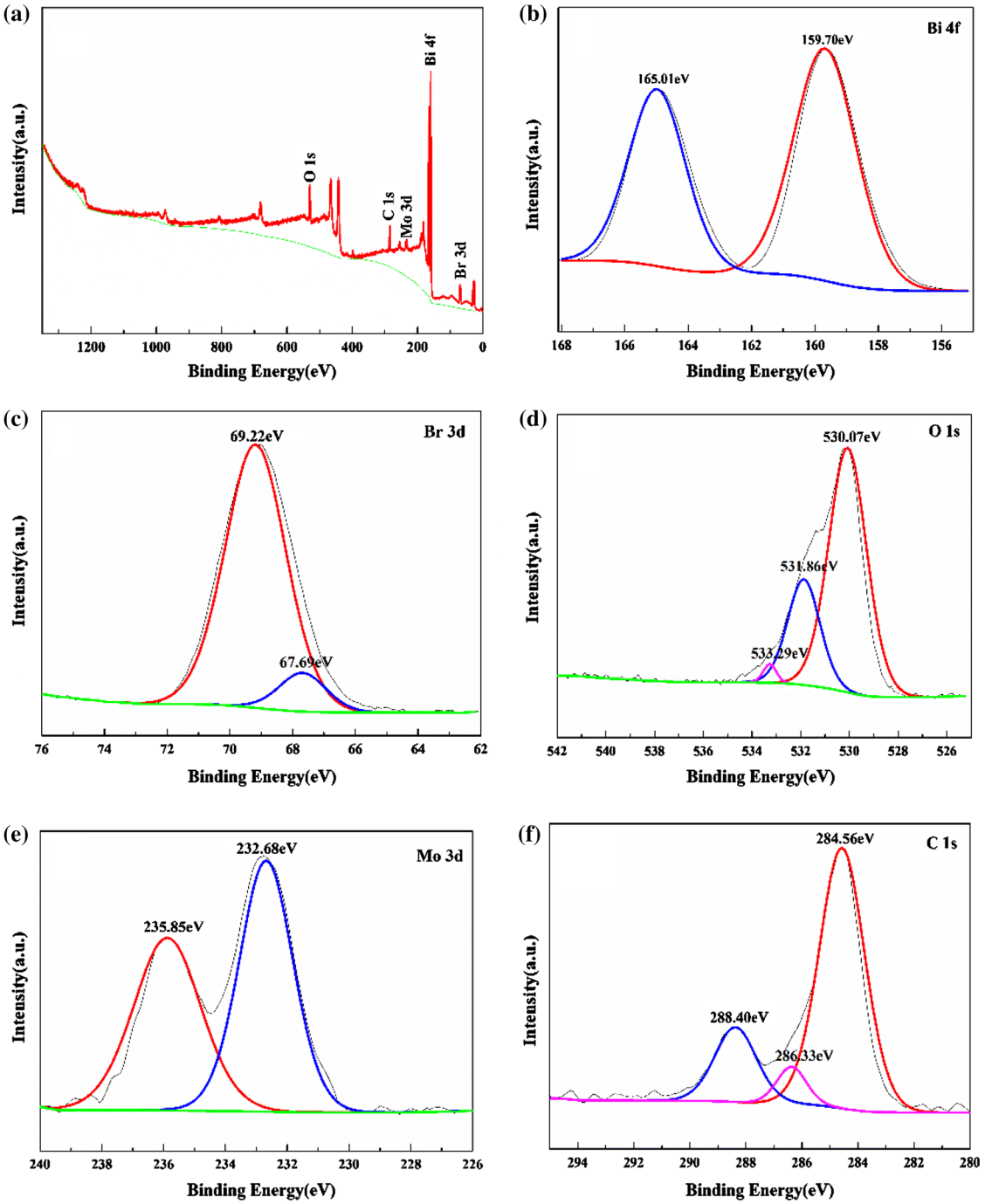

Figure 2 **a** XPS survey spectra of Bi_2MoO_6/RGO/BiOBr composite, **b** Bi 4*f*, **c** Br 3*d*, **d** O 1s, **e** Mo 3*d*, **f** C 1*s*.

corresponding to hydroxyl carbon (C–O), carbonyl carbon (C=O) and carboxyl carbon (O–C=O) [34], respectively. Generally speaking, the XPS spectroscopic analysis proves that Bi_2MoO_6/RGO/BiOBr composite catalyst has been successfully prepared in this experiment.

Micromorphology characterization

Scanning electron microscopy (SEM) is an important means to characterize the micro-surface morphology of the samples, and the surface morphology of the prepared photocatalysts is analyzed as shown in Fig. 3. Pure Bi_2MoO_6 is basically a sphere (Fig. 3a). As presented in Fig. 3b, it is easy to observe that BiOBr has the characteristics of three-dimensional layered microspheres with an average diameter of 0.625 nm, which is composed of a large number of petal-shaped two-dimensional nanosheets with gaps in the middle. Figure 3c displays that BiOBr layered microspheres are distributed on the surface of Bi_2MoO_6 spheres, leading to the formation of a heterostructure. For the Bi_2MoO_6/RGO/BiOBr composite (Fig. 3d), it can be clearly seen that BiOBr is evenly embedded around Bi_2MoO_6, and BiOBr still maintains a good morphology of microspheres. It can also be seen that RGO distributes between Bi_2MoO_6 and BiOBr, forming a Bi_2MoO_6/RGO/BiOBr structure with close contact interface, which can effectively accelerate the separation and migration of photocarriers on BiOBr surface during photocatalytic process.

TEM was also carried out in this study to further study the surface micromorphology of the samples. The results also confirm the conclusion of SEM that there is a close and large contact area between Bi_2MoO_6, RGO and BiOBr. Moreover, Fig. 4b also shows the HRTEM image of Bi_2MoO_6/RGO/BiOBr, from which we can clearly observe the close interfacial cross-linking structure among Bi_2MoO_6, RGO and BiOBr. The lattice fringe spacing of 0.31 nm and 0.425 nm are (012) and (110) planes of Bi_2MoO_6, respectively, and the lattice fringe spacing of 0.272 nm corresponds to (110) planes of BiOBr [32]. These different crystal planes also indicate that the

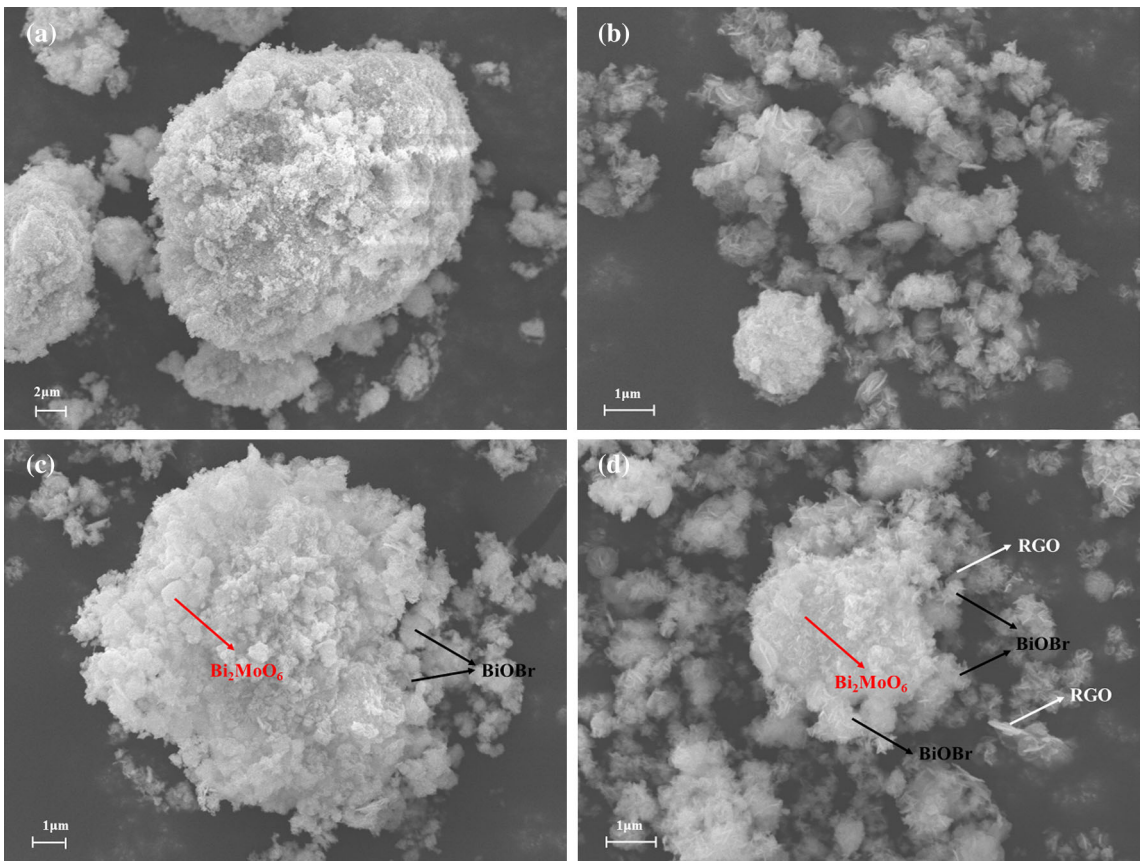

Figure 3 SEM image of Bi_2MoO_6 (**a**), BiOBr (**b**), Bi_2MoO_6/BiOBr (**c**) and Bi_2MoO_6/RGO/BiOBr (**d**).

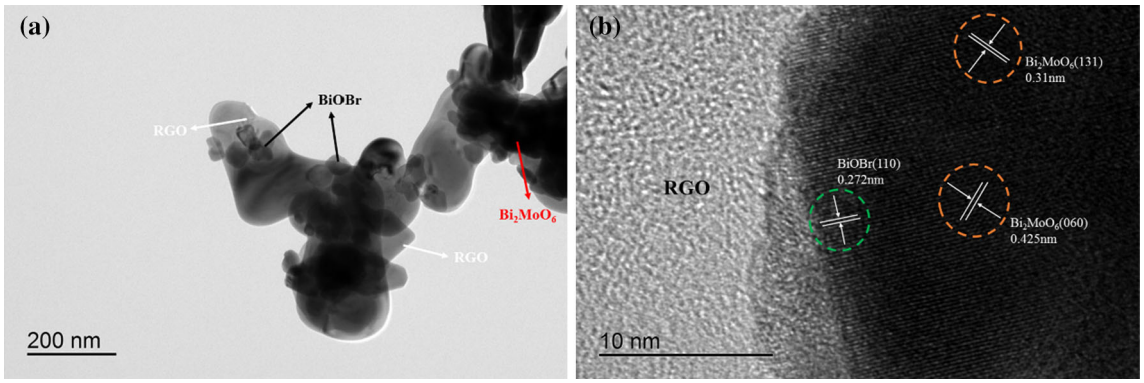

Figure 4 TEM (**a**) and HRTEM (**b**) image Bi_2MoO_6/RGO/BiOBr composite.

heterojunction between Bi_2MoO_6 and BiOBr is formed directly, thus, the combination mode is conducive to the separation and transfer of photogenic carriers, and further improves the photocatalytic activity.

Figure 5 shows the N_2 adsorption–desorption isotherms of BiOBr and Bi_2MoO_6/RGO/BiOBr. According to IUPAC classification, the samples have type IV isotherms with tiny hysteresis loops, which confirm the existence of mesoporous structure. Besides, Table 1 displays the BET surface areas of samples. It can be concluded that the BET surface area of Bi_2MoO_6/RGO/BiOBr (23.82 m^2/g) is higher than BiOBr (16.75 m^2/g), which has a larger specific surface area as well as can provide a large number of surface active sites and is conducive to enhancing the photocatalytic activity of Bi_2MoO_6/RGO/BiOBr composite.

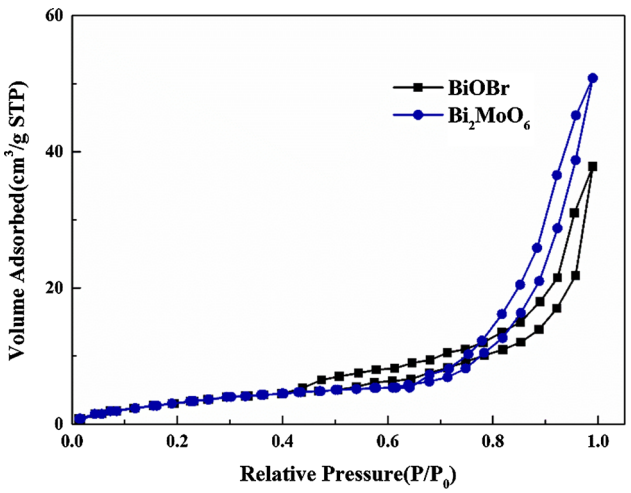

Figure 5 N_2 adsorption–desorption isotherms of BiOBr and Bi_2MoO_6/RGO/BiOBr.

Table 1 Textural properties of the samples

Sample	BET surface area (m^2/g)
BiOBr	16.75
Bi_2MoO_6/RGO/BiOBr	23.82

Optical absorption properties

UV–vis diffuse reflectance absorption is an important mean to characterize the energy level structure and visible-light absorption properties of semiconductor materials. The optical properties of BiOBr, Bi_2MoO_6, Bi_2MoO_6/BiOBr and Bi_2MoO_6/RGO/BiOBr composite were studied by UV–vis DRS. Figure 5 shows the UV–vis DRS of Bi_2MoO_6, BiOBr, Bi_2MoO_6/BiOBr and Bi_2MoO_6/RGO/BiOBr. The absorption band boundaries of Bi_2MoO_6 and BiOBr are about 550 nm and 480 nm, respectively, while the as-prepared 0.1Bi_2MoO_6/RGO/BiOBr exhibits light absorption almost in the whole visible spectrum, indicating that the formation of heterojunction greatly broadens the visible-light response range. In addition, the energy gap (E_g) of semiconductor material can be approximately calculated by using the following formula (2):

$$\alpha h\upsilon = A\left(h\upsilon - E_g\right)^{n/2} \quad (2)$$

where α, h, υ, E_g and A are absorption coefficient, Planck constant, optical frequency, bandgap and constant, respectively [35]. The value of n is 4 as BiOBr and Bi_2MoO_6 are both indirect bandgap semiconductors. Thus, the E_g values of BiOBr and Bi_2MoO_6 are calculated according to the plot of $(\alpha h\upsilon)^{1/2}$ versus energy ($h\upsilon$) as shown in Fig. 6b. The E_g values of BiOBr and Bi_2MoO_6 are 2.78 and 2.64 eV, respectively.

Visible-light absorption and photocatalytic activities

Methylene blue (MB) was chosen as the target pollutant in this study to evaluate the photocatalytic performance of Bi_2MoO_6/RGO/BiOBr heterojunction. Figure 7 shows the adsorption and photocatalytic degradation plots of MB by different catalysts. It can be seen that pure Bi_2MoO_6 and BiOBr have certain adsorption properties for MB, and the adsorption efficiency in dark is 11% and 32%, respectively. Besides, the adsorption rates of different Bi_2MoO_6 amounts (molar ratios are 0.05, 0.1, and 0.2) were 41.26%, 51.32% and 47.90%, respectively. The removal rates of MB by Bi_2MoO_6, BiOBr and Bi_2MoO_6/BiOBr after 30 min irradiation were 38.56%, 60.25% and 93.10%, respectively. For the Bi_2MoO_6/RGO/BiOBr composite, the removal rates were significantly improved under visible light, and the 96.93% of MB was degraded within 20 min. However, the dispersion of Bi_2MoO_6 on BiOBr surface will be affected when the amount of Bi_2MoO_6 is too high, which makes Bi_2MoO_6 become the composite center of electrons and holes, resulting in the reduction in the separation efficiency of photogenerated electron–hole pairs as well as the photocatalytic degradation. In addition, the photocatalytic comparative experiments of mechanical mixtures were carried out. The as-prepared Bi_2MoO_6/RGO/BiOBr composite has a higher degradation efficiency for MB compared with the mechanical mixture, which may be attributed to the formation of heterojunctions, thus contributing to the separation of photogenic carriers. The UV–vis absorption spectra (Fig. 7b) show the change in MB concentration with the increase in irradiation time during photocatalysis over 0.1Bi_2MoO_6/RGO/BiOBr composite. Moreover, the first-order kinetic equation expressed as $-\ln(C_t/C_0) = kt$ was used to study the photodegradation rate of catalytic samples, where C_t and C_0 are MB concentrations at t time and initial time, respectively, and k represents reaction rate constant (min^{-1}). The first-order kinetic plots as shown in Fig. 7c, the photodegradation rate of Bi_2MoO_6/BiOBr composite to MB (0.08348 min^{-1}) is higher than that of BiOBr (0.018 min^{-1}) and Bi_2MoO_6 (0.01265 min^{-1}), especially the Bi_2MoO_6/RGO/BiOBr composite exhibits the highest photodegradation efficiency. The k over Bi_2MoO_6/RGO/BiOBr is 7.23, 10.29 and 1.56 times higher than that of BiOBr, Bi_2MoO_6 and Bi_2MoO_6/BiOBr, respectively. Additionally, the mechanical mixed with the reaction rate constant of 0.01898 min^{-1} is similar to that of BiOBr, indicating that the interaction between the Bi_2MoO_6/RGO/BiOBr composite leads to the enhancement of photocatalytic performance.

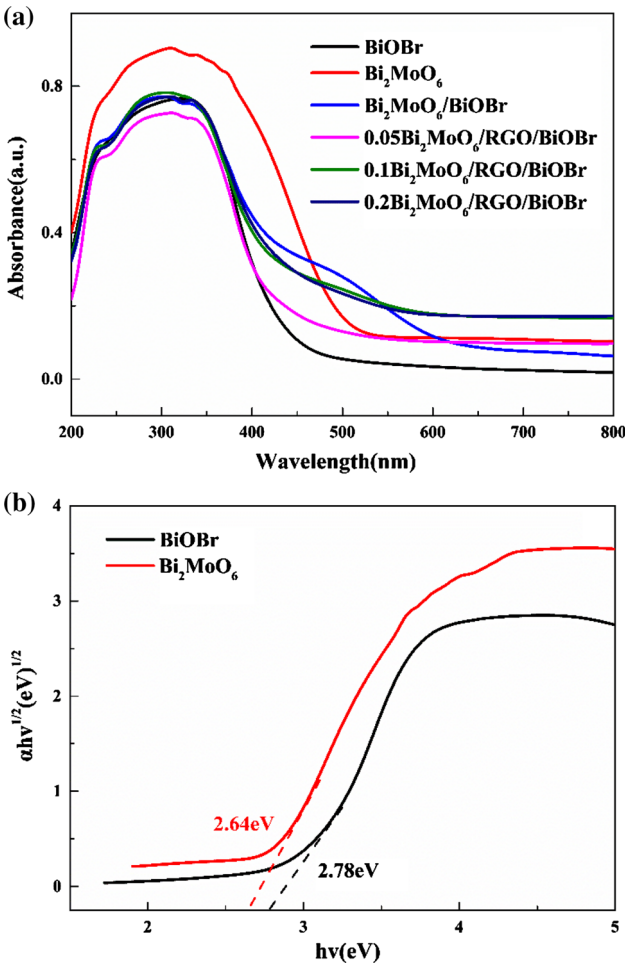

Figure 6 UV–vis DRS spectra of BiOBr, Bi_2MoO_6, Bi_2MoO_6/BiOBr and Bi_2MoO_6/RGO/BiOBr composite (**a**) and Kubelka–Munk plots of BiOBr and Bi_2MoO_6 (**b**).

The photocatalytic activities of Bi_2MoO_6, BiOBr, Bi_2MoO_6/BiOBr and Bi_2MoO_6/RGO/BiOBr were further studied by decomposing NFX solution under visible-light exposure, as shown in Fig. 7d. The degradation rate by Bi_2MoO_6/RGO/BiOBr is 78.12% after irradiation for 30 min, while that for BiOBr, Bi_2MoO_6 and Bi_2MoO_6/BiOBr composite are 21.5%, 19.98% and 61.03%, respectively. This is in good agreement with the results of MB removal that 0.1Bi_2MoO_6/RGO/BiOBr shows the best photocatalytic activity compared with other samples.

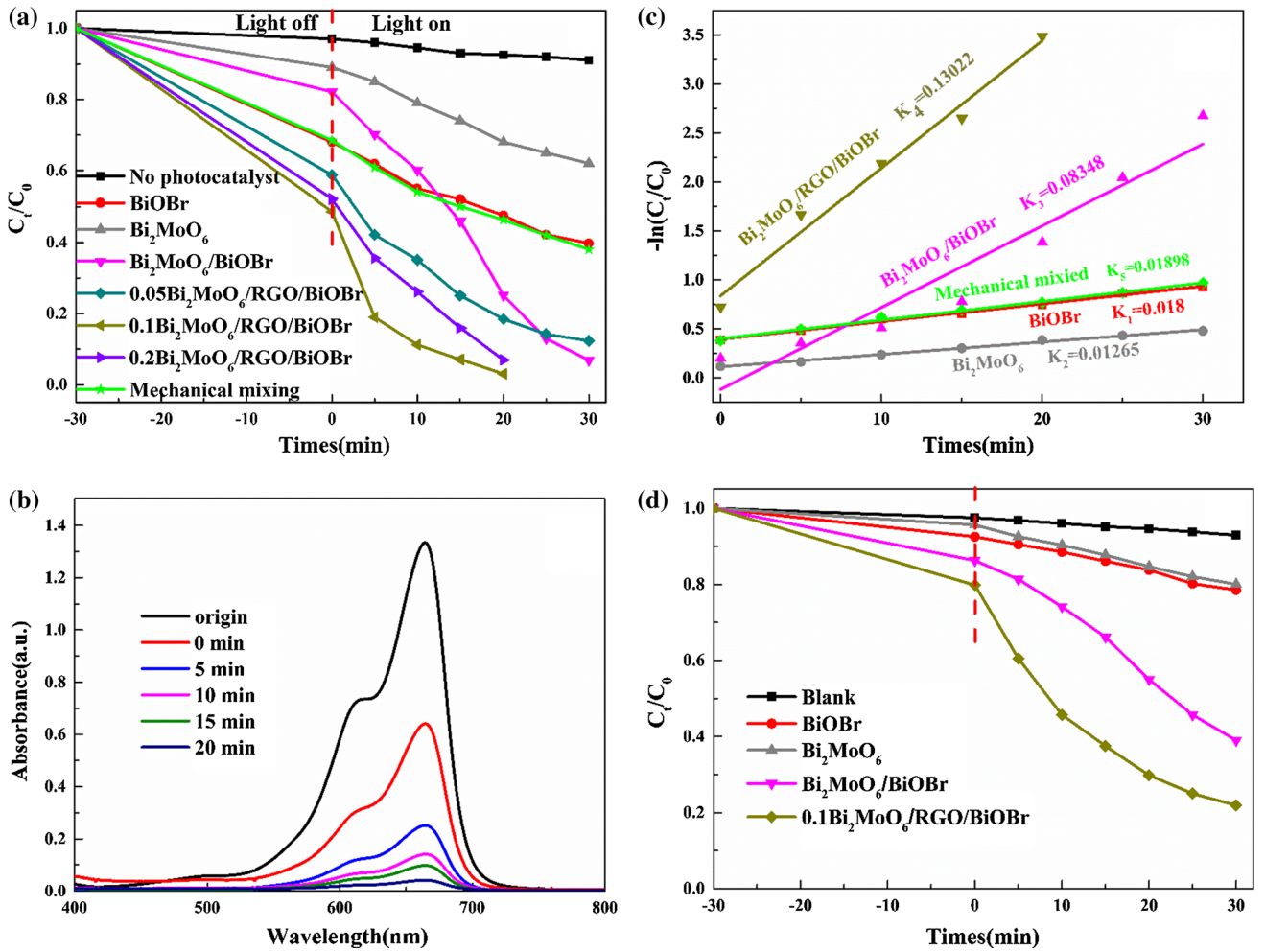

Figure 7 Photocatalytic degradation efficiencies of MB over different photocatalysts (**a**), Changes of UV–vis spectra of MB aqueous solution in the presence of $0.1Bi_2MoO_6$/RGO/BiOBr (**b**), the apparent pseudo-first-order t plot of $-\ln(C_t/C_0)$ for the photodegradation of MB (**c**) and photodegradation curves of NFX under visible-light irradiation (**d**).

Photocatalytic reaction mechanism

The efficiency of migration and separation of photogenerated electron–holes in composite photocatalysts play an important part in the photocatalytic reactions [23]. Firstly, the recombination of photogenerated electron–hole pairs was tested by photoluminescence spectroscopy. The peak intensity corresponds to the recombination degree of electron–hole pairs in the PL spectroscopy. Generally, the higher peak intensity indicates the higher recombination rate of electron–hole pairs [36]. Figure 8a is the PL spectroscopy of photocatalysts with an excitation wavelength of 325 nm. Pure BiOBr exhibits the highest fluorescence intensity, indicating that photogenerated electron–hole pairs produced by photoexcitation are easier to recombine. The fluorescence intensity of Bi_2MoO_6/BiOBr decreases slightly after the adjunction of Bi_2MoO_6, which indicates that the heterojunction interface can effectively separate photogenerated electron–hole pairs. There is no doubt that Bi_2MoO_6/RGO/BiOBr exhibits the weakest photofluorescence intensity, indicating that the photogenerated electron–hole pairs have the lowest recombination degree. The result shows that the introduction of RGO provides a faster carrier transfer path, which makes it difficult to recombine the photogenerated electron–hole pairs, thus facilitating the separation of electron–hole pairs in Bi_2MoO_6/RGO/BiOBr composite [37]. Therefore, Bi_2MoO_6/RGO/BiOBr composite can produce more active groups which can oxidize and degrade more organic pollutant, exhibiting a stronger photocatalytic activity.

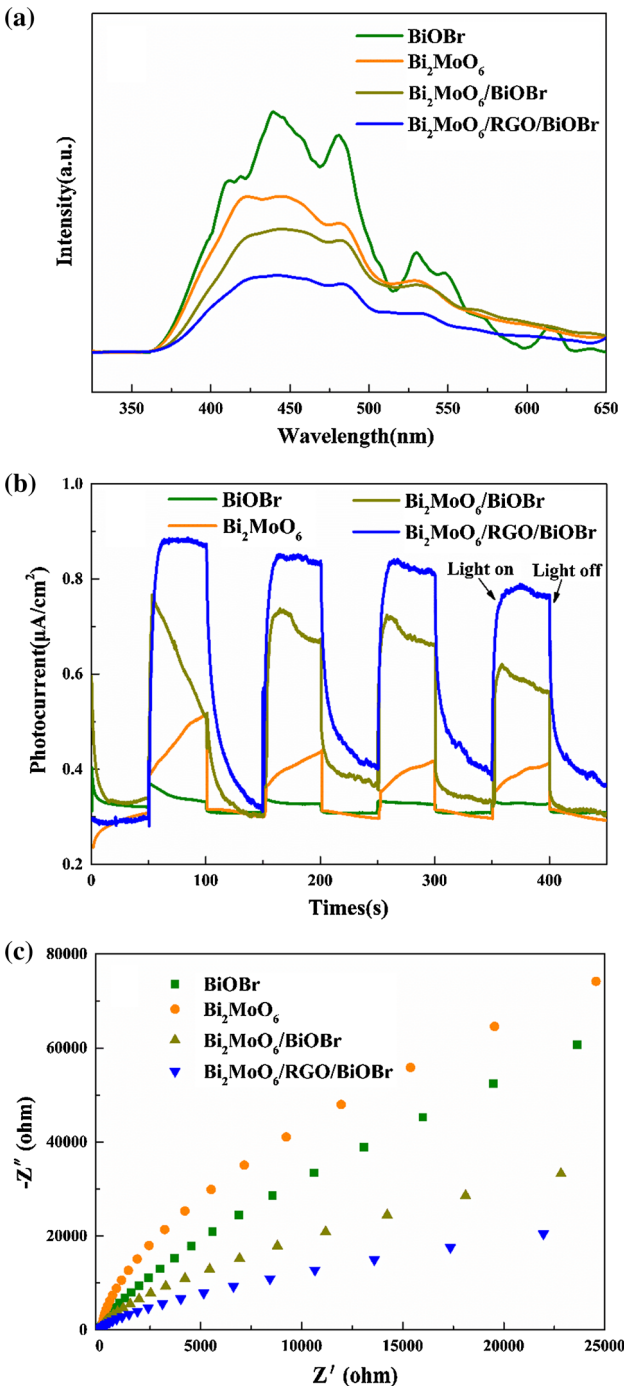

Figure 8 Photoluminescence spectra (**a**), photocurrent response spectra (**b**) and EIS Nyquist plots (**c**) of Bi_2MoO_6, BiOBr, Bi_2MoO_6/BiOBr and Bi_2MoO_6/RGO/BiOBr composite.

The transient photocurrent experiments of pure BiOBr, Bi_2MoO_6, Bi_2MoO_6/BiOBr and Bi_2MoO_6/RGO/BiOBr composite photocatalysts were also carried out in order to study the separation efficiency of photogenerated electron–holes under visible-light exposure. The sample electrodes both have a fast photocurrent response whenever the switch is turned on or off. Figure 8b shows that Bi_2MoO_6/RGO/BiOBr composite photocatalyst exhibits stronger photocurrent response than pure BiOBr and Bi_2MoO_6. Because the photocurrent is the current formed in the process of transferring photogenerated electrons from valence band to conduction band under visible light, the higher photocurrent intensity suggests the faster transmission speed of photogenerated electrons, that is, the higher separation efficiency between photogenerated electrons and holes. This means that the three-phase heterojunction structure in Bi_2MoO_6/RGO/BiOBr composite is more conducive to the separation and transfer of photogenerated carriers.

Moreover, the electrochemical impedance spectroscopy (EIS) of the as-prepared photocatalysts was carried out to discuss the electron transfer process. The electrochemical impedance radius reflects the charge transfer resistance occurring at the interface between the working electrode and the electrolyte solution. Generally, the smaller electrochemical impedance radius suggesting the smaller the charge transfer resistance [38]. As shown in Fig. 8c, the arc radius of Bi_2MoO_6/RGO/BiOBr composite photocatalyst is smallest, which means that the resistance of charge transfer at the interface of the composite photocatalyst is smallest and the transfer rate is fastest, thus further realizing the effective separation of photogenerated electron holes. The EIS results are consistent with the results of photocurrent analysis that an efficient electron transport system has been constructed on the interface between Bi_2MoO_6/RGO and BiOBr, accelerating the transmission efficiency of photogenerated electron–hole separation of Bi_2MoO_6/RGO/BiOBr composite photocatalyst as well as improving its photocatalytic activity.

A series of free radical trapping experiments were carried out to detect the primary active species in photocatalytic reaction, so as to further explore the photocatalytic mechanism of Bi_2MoO_6/RGO/BiOBr composite photocatalyst. Figure 9a shows that the photocatalytic activity of Bi_2MoO_6/RGO/BiOBr is greatly inhibited after adding 1 mmol BQ and EDTA-2Na separately to the reaction system, while the catalytic performance is slightly affected after adding 10 mmol IPA. The photodegradation rate decreased from 96.93% to 54.79%, 57.91% and 91.02%, respectively, after adding BQ, EDTA-2Na and IPA. It can be

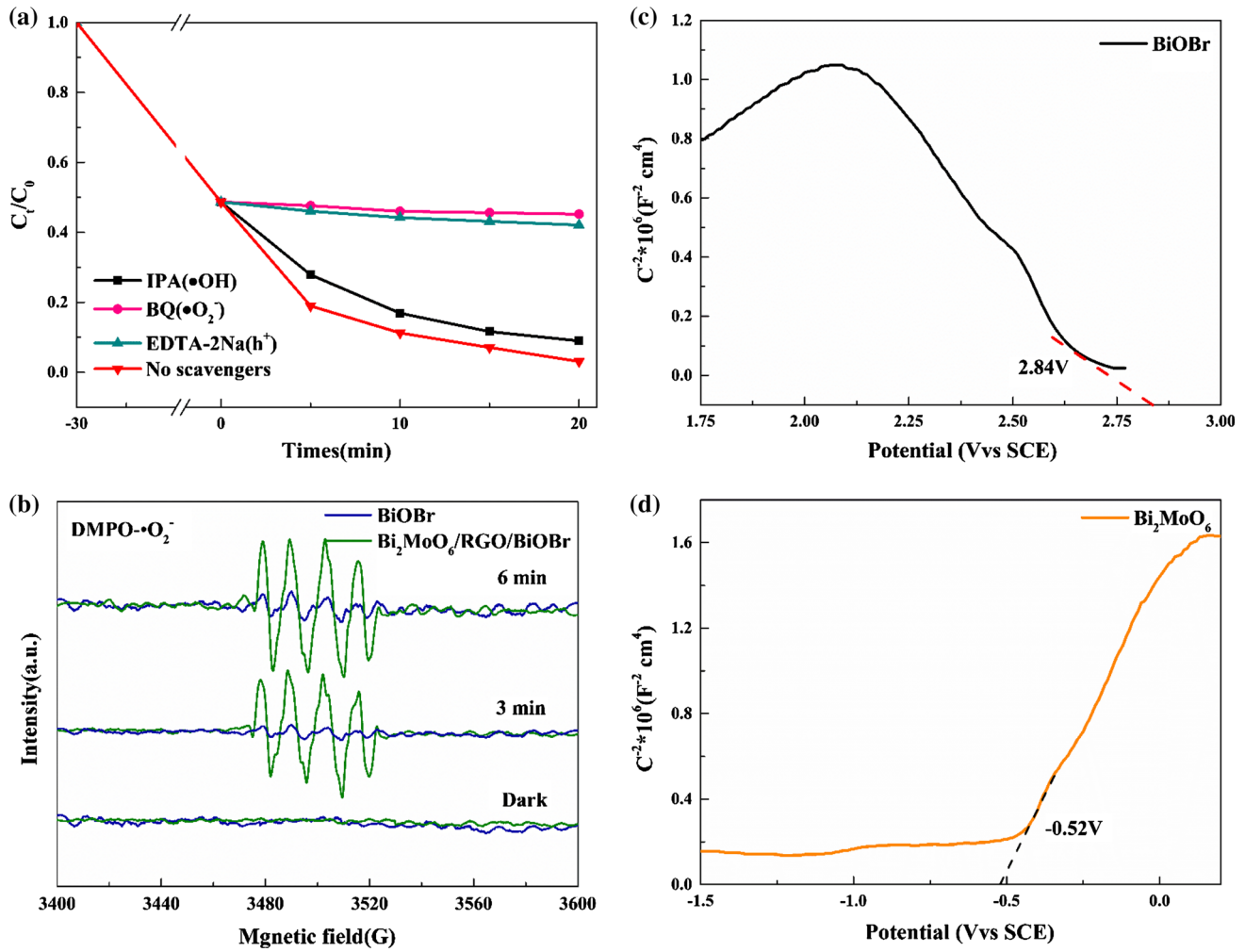

Figure 9 Degradation plot of MB by adding IPA, BQ and EDTA-2Na to Bi_2MoO_6/RGO/BiOBr composite catalyst (**a**), ESR spectra of DMPO-•O_2^- in methanol dispersions recorded with BiOBr and Bi_2MoO_6/RGO/BiOBr (**b**), Mott–Schottky plots of BiOBr (**c**) and Bi_2MoO_6 (**d**).

concluded that holes (h^+) and superoxide anions (•O_2-) play a major role and •OH plays a negligible part in the photocatalytic degradation by Bi_2MoO_6/RGO/BiOBr composite. Additionally, the electron spin resonance (ESR) measurements of BiOBr and Bi_2MoO_6/RGO/BiOBr photocatalysts are taken under visible-light irradiation to further study its degradation mechanism. As shown in Fig. 9b, no signals of DMPO-•O_2^- for BiOBr and Bi_2MoO_6/RGO/BiOBr composite are detected in dark. After 3 min visible-light irradiation, the four characteristic peaks of DMPO-•O_2^- are observed and the peak intensities gradually increase with the increase in time. It is obvious that the signal intensity of DMPO-•O_2^- for Bi_2MoO_6/RGO/BiOBr composite is much stronger than that for BiOBr, which indicates that more •O_2^- radicals can be generated in Bi_2MoO_6/RGO/BiOBr composite due to Z-scheme electron transfer mechanism.

It is well known that the relative position of VB and CB of photocatalysts will affect the redox ability of photogenerated electrons and holes in semiconductors, and then affect their photocatalytic activity. The flat-band potentials (U_{fb}) of BiOBr and Bi_2MoO_6 were analyzed by Mott–Schottky [39] plots in this paper, and the relative positions of VB and CB are calculated. As shown in Fig. 9b, the negative slope of *M–S* plot for BiOBr indicates that it is a *p*-type semiconductor. The U_{fb} of BiOBr is 2.84 V (vs. SCE) which is estimated using the horizontal axis intercept of the *M–S* plots, so the VB value of BiOBr is 2.84 V (SCE, VB ≈ U_{fb}) [40]. Then, the value of VB is 3.08 V

relative to the normal hydrogen electrode (NHE, NHE = SCE + 0.24 V) [41]. As shown in Fig. 9c, the positive slope of the *M–S* plot of Bi_2MoO_6 indicating that it is an n-type semiconductor. The U_{fb} value of Bi_2MoO_6 is − 0.52 V (vs. SCE), and then, the CB value of Bi_2MoO_6 is − 0.72 V (CB ≈ U_{fb} − 0.2 V) [42]; thus the value of CB is − 0.48 V relative to the normal hydrogen electrode (NHE, NHE = SCE + 0.24 V). Furthermore, the E_g of BiOBr and Bi_2MoO_6 are 2.78 eV and 2.64 eV, respectively, according to the results of UV–vis DRS, and thus the CB potential of BiOBr is 0.30 eV versus NHE and the VB potential of Bi_2MoO_6 is 2.16 eV versus NHE, respectively, which can be calculated by $E_g = E_{VB} - E_{CB}$.

This study proposes a Z-scheme charge transfer mechanism suitable for the Bi_2MoO_6/RGO/BiOBr system as shown in Fig. 10 based on the experimental results of free radical capturing and the structural analysis of semiconductor CB and VB potentials. Actually, the electrons in the valence band (VB) of BiOBr are excited and transferred to the conduction band (CB) under visible-light irradiation. The electrons in the CB of BiOBr can rapidly migrate to the VB of Bi_2MoO_6 through RGO and recombine with the holes because of the good conductivity of RGO. Then, the electrons and holes are gathered in the CB of Bi_2MoO_6 and the VB of BiOBr, respectively, and thus, the recombination of electrons and holes is effectively inhabited. These electrons can react with O_2 adhering to the catalyst surface to produce $\bullet O_2^-$ to degrade organic pollutants since the CB potential of Bi_2MoO_6 (−0.48 eV) is less negative than that of $O_2/\bullet O_2^-$ (− 0.33 eV) [43]. Besides, the photogenic holes gathered in VB of BiOBr are more oxidative and can selectively decompose pollutants directly. Therefore, the heterostructure of BiOBr and Bi_2MoO_6 taking RGO as electronic modifier accelerates the photoinduced electron transfer between BiOBr and Bi_2MoO_6, and then, the electron–hole pairs are effectively separated, thus improving the performance of Bi_2MoO_6/RGO/BiOBr photocatalyst. The photocatalytic process can be described as follows:

Absorption of photons:

$$Bi_2MoO_6 + BiOBr + h\nu \rightarrow Bi_2MoO_6(e^- + h^+) + BiOBr(e^- + h^+)$$

Photogenerated electrons transfer through RGO sheets:

$$Bi_2MoO_6(e^- + h^+) + BiOBr(e^- + h^+) \rightarrow Bi_2MoO_6(e^-) + BiOBr(h^+)$$

Reduction of oxygen:

$$O_2 + Bi_2MoO_6(e^-) \rightarrow Bi_2MoO_6 + \cdot O_2^-$$

Degradation of pollutants:

$$\cdot O_2^- + \text{pollutants} \rightarrow \text{degradation products}(CO_2 + H_2O)$$

$$BiOBr(h^+) + \text{pollutants} \rightarrow BiOBr + \text{degradation products}(CO_2 + H_2O)$$

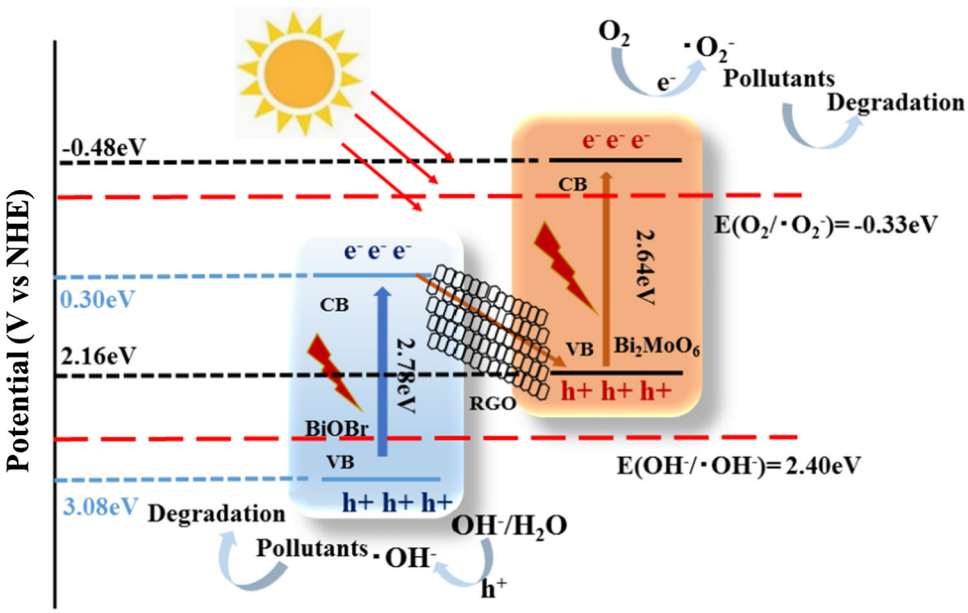

Figure 10 Proposed Z-scheme charge transfer of Bi_2MoO_6/RGO/BiOBr system.

Conclusions

In summary, the novel Bi_2MoO_6/RGO/BiOBr composite was successfully synthesized via a facile solvothermal synthesis and precipitation method in this study. The structural, micromorphology and optional property of the as-prepared samples were analyzed by XRD, XPS, SEM, TEM and UV–vis DRS. The photocatalytic activity of the photocatalyst under visible-light irradiation was investigated taking MB and NFX as degradation target. The Z-scheme mechanism of photocatalytic degradation for Bi_2MoO_6/RGO/BiOBr composite was deduced by UV–Vis DRS spectra, *M–S* curves and free radical capture experiments. This study provides a promising platform for efficient catalytic applications in photocatalytic degradation of pollutants and environmental remediation.

Compliance with ethical standards

Conflict of interest The authors declare that they have no conflict of interest.

References

[1] Lin H (1999) The study of oxygen spillover and back spillover on Pt/TiO_2 by a potential dynamic sweep method. Mol Catal 144(1):189–197

[2] Legrini O, Oliveros E, Braun A-M (1993) Photochemical processes for water treatment. Chem Rev 93(2):671–698

[3] Wei X-X, Chen C-M, Guo S-Q et al (2014) Advanced visible-light-driven photocatalyst BiOBr–TiO_2–graphene composite with graphene as a nano-filler. J Mater Chem A 2(13):4667–4675

[4] Zhang M, Shao C, Mu J et al (2011) One-dimensional Bi_2MoO_6/TiO_2 hierarchical heterostructures with enhanced photocatalytic activity. CrystEngComm 14(2):605–612

[5] Zhao S, Chen S, Yu H, Quan X (2012) g-C_3N_4/TiO_2 hybrid photocatalyst with wide absorption wavelength range and effective photogenerated charge separation. Sep Purif Technol 99(8):50–54

[6] Shang M, Wang W, Zhang L (2009) Preparation of BiOBr lamellar structure with high photocatalytic activity by CTAB as Br source and template. J Hazard Mater 167(1):803–809

[7] Huo Y, Zhang J, Dai K, Li Q, Liang C (2019) All-solid-state artificial Z-scheme porous g-C_3N_4/Sn_2S_3-DETA heterostructure photocatalyst with enhanced performance in photocatalytic CO_2 reduction. Appl Catal B Environ 241:528–538

[8] Li Z, Wang X, Zhang J, Liang C, Lu L, Dai K (2019) Preparation of Z-scheme $WO_3(H_2O)0.333$/Ag_3PO_4 composites with enhanced photocatalytic activity and durability. Chin J Catal 40(3):326–334

[9] Lv J, Zhang J, Liu J, Li Z, Dai K, Liang C (2017) Bi SPR-promoted Z-scheme Bi_2MoO_6/CdS-diethylenetriamine composite with effectively enhanced visible light photocatalytic hydrogen evolution activity and stability. ACS Sustain Chem Eng 6(1):696–706

[10] Wang Z, Lv J, Zhang J, Dai K, Liang C (2017) Facile synthesis of z-scheme $BiVO_4$/porous graphite carbon nitride heterojunction for enhanced visible-light-driven photocatalyst. Appl Surf Sci 430:595–602

[11] Zhang S, Wang D (2015) Preparation of novel BiOBr/CeO_2 heterostructured photocatalysts and their enhanced photocatalytic activity. RSC Adv 5(113):93032–93040

[12] Xing Y, He Z, Que W (2016) Synthesis and characterization of ZnO nanospheres sensitized BiOBr plates with enhanced photocatalytic performances. Mater Lett 182:210–213

[13] Shan L, Liu Y, Chen H (2017) An α-Bi_2O_3/BiOBr core–shell heterojunction with high photocatalytic activity. Dalton Trans 46(7):2310

[14] Tian G, Chen Y, Zhou W et al (2010) Facile solvothermal synthesis of hierarchical flower-like Bi_2MoO_6 hollow spheres as high performance visible-light driven photocatalysts. J Mater Chem 21(3):887–892

[15] Tian Y, Cheng F, Xiang Z et al (2014) Solvothermal synthesis and enhanced visible light photocatalytic activity of novel graphitic carbon nitride-Bi_2MoO_6 heterojunctions. Powder Technol 267(15):126–133

[16] Xu Y, Zhang W (2013) Monodispersed Ag_3PO_4 nanocrystals loaded on the surface of spherical Bi_2MoO_6 with enhanced photocatalytic performance. Dalton Trans 42(4):1094–1101

[17] Hu T, Yang Y, Dai K, Zhang J, Liang C (2018) A novel Z-scheme Bi_2MoO_6/BiOBr photocatalyst for enhanced photocatalytic activity under visible light irradiation. Appl Surf Sci 456(31):473–481

[18] Wang Z, Hu T, Dai K, Zhang J, Liang C (2017) Construction of Z-scheme Ag_3PO_4/Bi_2WO_6 composite with excellent visible-light photodegradation activity for removal of organic contaminants. Chin J Catal 38(12):2021–2029

[19] Lv J, Dai K, Zhang J, Lu L, Liang C, Geng L et al (2017) In situ controllable synthesis of novel surface plasmon resonance-enhanced Ag_2WO_4/Ag/Bi_2MoO_6 composite for enhanced and stable visible light photocatalyst. Appl Surf Sci 391:507–515

[20] Zhang R, Cai Y, Zhu X (2019) A novel photocatalytic membrane decorated with PDA/RGO/Ag_3PO_4 for catalytic dye decomposition. Colloid Surface A 563:68–76

[21] Zhang Y, Zhu Y, Yu J (2013) Enhanced photocatalytic water disinfection properties of Bi_2MoO_6–RGO nanocomposites under visible light irradiation. Nanoscale 5(14):6307–6310

[22] Chen P-L, Chen I-W (2010) Reactive cerium (IV) oxide powders by the homogeneous precipitation method. J Am Ceram Soc 76(6):1577–1583

[23] Wang S, Yang X, Zhang X (2017) A plate-on-plate sandwiched Z-scheme heterojunction photocatalyst: BiOBr–Bi_2MoO_6 with enhanced photocatalytic performance. Appl Surf Sci 391:194–201

[24] Fu Y, Chen H, Sun X, Wang X (2012) Combination of cobalt ferrite and graphene: highperformance and recyclable visible-light photocatalysis. Appl Catal B Environ 111–112:280–287

[25] Qiu F, Li W, Wang F et al (2017) In-situ synthesis of novel Z-scheme SnS_2/BiOBr photocatalysts with superior photocatalytic efficiency under visible light. J Colloid Interface Sci 493:1–9

[26] Kong L, Jiang Z, Xiao T (2011) Exceptional visible-light-driven photocatalytic activity over BiOBr–$ZnFe_2O_4$ heterojunctions. Chem Commun 47(19):5512–5514

[27] Xie L-J, Ma J-F, Xu G-J (2008) Preparation of a novel Bi_2MoO_6 flake-like nanophotocatalyst by molten salt method and evaluation for photocatalytic decomposition of rhodamine B. Mater Chem Phys 110(2–3):197–200

[28] Chen F, Yang Q, Li X et al (2017) Hierarchical assembly of graphene-bridged Ag_3PO_4/Ag/$BiVO_4$ (040) Z-scheme photocatalyst: An efficient, sustainable and heterogeneous catalyst with enhanced visible-light photoactivity towards tetracycline degradation under visible light irradiation. Appl Catal B Environ 200:330–342

[29] Liu Y, Yang ZH, Song PP et al (2018) Facile synthesis of Bi_2MoO_6/$ZnSnO_3$ heterojunction with enhanced visible light photocatalytic degradation of methylene blue. Appl Surf Sci 430:561–570

[30] Li H, Li W, Wang F, Liu F et al (2018) Fabrication of Pt nanoparticles decorated Gd-doped Bi_2MoO_6 nanosheets: design, radicals regulating and mechanism of Gd/Pt–Bi_2MoO_6 photocatalyst. Appl Surf Sci 427:1046–1053

[31] Xu Y-S, Zhang W-D et al (2013) Anion exchange strategy for construction of sesame-biscuit-like $Bi_2O_2CO_3$/Bi_2MoO_6 nanocomposites with enhanced photocatalytic activity. Appl Catal B Environ 140–141(8):306–316

[32] Zhang M, Shao C, Mu J, Zhang Z et al (2012) One-dimensional Bi_2MoO_6/TiO_2 hierarchical heterostructures with enhanced photocatalytic activity. CrystEngComm 14:605–612

[33] Wang Z, Zhang J, Lv J, Dai K, Liang C (2017) Plasmonic Ag_2MoO_4/AgBr/Ag composite excellent photocatalytic performance and possible photocatalytic mechanism. Appl Surf Sci 396:791–798

[34] Meng X, Zhang Z (2016) Plasmonic ternary Ag–rGO–Bi_2MoO_6 composites with enhanced visible light-driven photocatalytic activity. J Catal 344:616–630

[35] Luo Y, Huang Q, Li B et al (2017) Synthesis and characterization of Cu_2O-modified Bi_2O_3 nanospheres with enhanced visible light photocatalytic activity. Appl Surf Sci 357:1072–1079

[36] Ma D, Wu J, Gao M, Xin Y, Chai C (2017) Enhanced debromination and degradation of 2, 4-dibromophenol by an Z-scheme Bi_2MoO_6/CNTs/g-C_3N_4 visible light photocatalyst. Chem Eng J 316:461–470

[37] Jia Y, Ma Y, Tang J, Shi W (2018) Hierarchical nanosheet-based Bi_2MoO_6 microboxes for efficient photocatalytic performance. Dalton Trans 47:5542–5547

[38] Shi Q, Zhao W, Xie L et al (2016) Enhanced visible-light driven photocatalytic mineralization of indoor toluene via a $BiVO_4$/reduced graphene oxide/Bi_2O_3 all-solid-state Z-scheme system. J Alloys Compd 662:108–117

[39] Xu B, He P, Liu H et al (2014) A 1D/2D helical CdS/$ZnIn_2S_4$ nano-heterostructure. Angew Chem Int Ed 126:2339–2343

[40] Song S, Meng A, Jiang S, Cheng B, Jiang C (2017) Construction of Z-scheme Ag_2CO_3/N-doped graphene photocatalysts with enhanced visible-light photocatalytic activity by tuning the nitrogen species. Appl Surf Sci 396:1368–1374

[41] Xu D, Cheng B, Wang W et al (2018) Ag_2CrO_4/g-C_3N_4/-graphene oxide ternary nanocomposite Z-scheme photocatalyst with enhanced CO_2, reduction activity. Appl Catal B Environ 231:368–380

[42] Cai T, Liu Y, Wang L, Zhang S et al (2017) Silver phosphate-based Z-scheme photocatalytic system with superiorsunlight photocatalytic activities and anti-photocorrosion performance. Appl Catal B Environ 208:1–13

[43] Liu Y, Wang R, Yang Z et al (2015) Enhanced visible-light photocatalytic activity of Z-scheme graphitic carbon nitride/oxygen vacancy-rich zinc oxide hybrid photocatalysts. Chin J Catal 36(12):2135–2144